Numerical Characterization of a Liquid Metal Magnetohydrodynamic Alternate Generator in the Laminar-Regime under Inductionless Approximation

J. A. Rizzo Sierra[†], C. Isaza, J. P. Zavala de Paz, E. K. Anaya Rivera

Polytechnic University of Querétaro. State Street 420 W/N. P. O. box code 76240. The Marquis, Querétaro, México.

† *Corresponding Author Email: amilcar.rizzo@gmail.com*

ABSTRACT

The performance characterization of a liquid metal magnetohydrodynamic alternate generator is numerically investigated via its electric isotropic efficiency. The model consists of a harmonically driven liquid metal oscillatory flow confined to a thin-walled closed rectangular duct interacting with a uniform magnetic field transverse to its motion and attached to a load resistance. Spectral collocation method is used to solve the properly boundary-conditioned Navier-Stokes equation under inductionless approximation for the magnetic field with implementation of gradient formulation for the electric field. Flow is considered fully developed in the direction perpendicular to the applied uniform magnetic field (i.e., motion direction), incompressible, viscous, and laminar in regime. Currently, there are neither purely analytical or experimental results on this problem, but ours were cross-referenced with those from a one-dimensional analytical model as close as possible to it, finding reasonable correspondence. Dimensional estimates on the power production of prospective mesoscale devices having in mind household application are provided for different liquid metals as well.

Keywords: Magnetohydrodynamics; Oscillatory liquid metal flow; Laminar fully developed regime; Inductionless approximation; Navier-Stokes equation; Spectral collocation method; Alternative power generation.

1. INTRODUCTION

Flow features and/or performance of liquid metal magnetohydrodynamic (LM-MHD) generators is an important subject to both pure and applied physics. Over time, it has been approached experimentally Ishikawa *et al*. (1996), Nomura (1988), Intani *et al*. (2010), Kobayashi *et al*. (2011), Liu *et al*. (2011), Shionoya *et al*. (2011), Liu *et al*. (2014), Niu *et al*. (2014), numerically for the steady situation Yamada *et al.* (2007), Yamada *et al.* (2006), analytically Jackson (1963), Ibáñez *et al.* (2002), Vogin *et al.* (2007), and in combinations of the previous Satyamurthy *et al.* (1999), Danilyan *et al.* (2005), Yamaguchi *et al.* (2011). Analytical approaches for the LM-MHD generator are generally difficult. But that hasn't prevented development of approximations, mainly based on Faraday and Hartmann generator models. Accounts on the former and Hartmann flow (with its own feasibility to be implemented as a generator model too) can be found in Davidson (2001), Müller *et al.* (2001). Some authors further simplify modeling by not using energy and/or Navier-Stokes Hu *et al.* (2015). Studies using Faraday's

model can be found in Koslover *et al.* (2007) for a device patent, Jackson (1963) for the DC case, and Ibáñez *et al,* (2002) using Hartmann's flow model under inductionless approximation to view the setup as a one-dimensional $(1 -D)$ Faraday alternate generator. An application of the Hartmann generator model can be found in Vogin *et al.* (2007). In this paper, a physical/numerical formulation having as antecedents the studies of steady and oscillatory LM-MHD flows respectively by Cuevas (1994), Cuevas *et al.* (1997) and Rizzo-Sierra (2017), Rizzo-Sierra *et al.* (2016), is developed to characterize the performance of a LM-MHD alternate generator. Flow is considered completely developed, incompressible, viscous, laminar and inductionless. Considerations on the harmonic pressure gradient driving the system are outside its scope. The harmonic pressure gradient can be obtained by the thermoacoustic effect Migliori *et al.* (1988), Swift (1988). For the parametric ranges explored on section 7, these systems could need a frequency coupling stage, intermediate between the thermo-acoustic machine and the LM-MHD transducer/generator. Paper distribution: some remarks on the physical formulation of the problem

are made in section 2 below. In section 3, summaries on the thin wall approximation, Hartmann layer contribution to the electric current within the fluid, and load resistance attachment model are given. In section 4, a summary on the spectral collocation numerical formulation is introduced. In section 5, a comparison between our numerically obtained efficiencies and results of a one-dimensional $(1 - D)$ LM-MHD inductionless generator analytical model is conducted. In section 6, results are presented and discussed in terms of dimensionless parameters defining the problem. Concluding remarks with dimensional estimates on the power of prospective devices for household application with different liquid metals are shown in section 7. Finally, Appendix A provides details on the analytical expressions used in section 5.
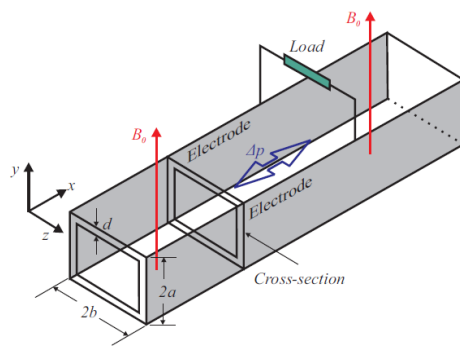

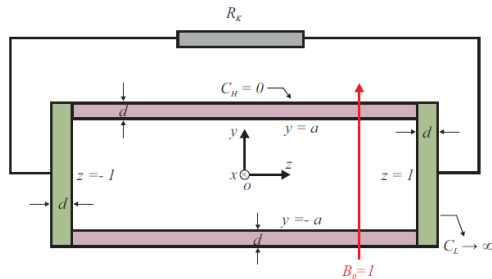**Fig. 1. Schematic of the generator setup.**

Fig. 2. Generator dimensionless cross-section.

2. PHYSICAL FORMULATION

It deals with the functioning of a LM-MHD electric generator by attaching a load resistance to a rectangular duct holding an electrically conducting oscillatory flow interacting with a magnetic field in the inductionless approximation. This problem is along the lines of Rizzo-Sierra (2017), Rizzo-Sierra *et al.* (2016). They deal with similar systems from the magnetohydrodynamics standpoint, without a load resistance attachment and other particularities an electrical generator requires. These imply solving the Navier-Stokes equation with a harmonically driven, incompressible, electrically conducting, laminar, completely developed, and viscous flow through a thin-walled duct of rectangular cross-section —Figs. 1, 2—. Flow interacts with a uniform magnetic field traverse to it, and is connected to a load resistance (R_K). Duct

conductivities are considered null and tending to infinite for Hartmann (perpendicular to applied magnetic field) and lateral walls (parallel to it) respectively. That way, functional dependence in the Cartesian coördinate system of all variables lies in y, z, while t denotes time. $\vec{u} = u_x\,(y,\ z,\ t)\ \hat{e}_x$ defines velocity, and $\hat{e}_x$ is x direction unit vector. Readers are encouraged to consult those references for details on the basic physical magneto-hydrodynamic formulation. Then they can continue reviewing the load resistance attachment component of it within this paper's section 3. Previous considerations conduce to equations and boundary conditions in terms of F and F_w, fluid and wall regions electric stream current functions, respectively. Before de-coupling them, the formulation results: a) Equations

$$M^{-2}\left(\frac{\partial^2 u_0}{\partial y^2} + \frac{\partial^2 u_0}{\partial z^2}\right) - \frac{\partial^2 F}{\partial y^2} - iN_\omega^{-1}u_0 = G \qquad (1)$$

Within the fluid region ($0 < y < a \wedge 0 < z < 1$):

$$u_0 = \frac{\partial^2 F}{\partial y^2} + \frac{\partial^2 F}{\partial z^2} \qquad (2)$$

At the duct walls ($a < y < a + d \wedge 0 < z < 1 + d$; $0 < y < a + d \wedge 1 < z < 1 + d$):

$$\frac{\partial^2 F_w}{\partial y^2} + \frac{\partial^2 F_w}{\partial z^2} = 0 \qquad (3)$$

b) Boundary conditions: At $z = 0$:

$$\frac{\partial}{\partial z}\left(\frac{\partial^2 F}{\partial y^2} + \frac{\partial^2 F}{\partial z^2}\right) = 0,\ \frac{\partial F}{\partial z} = 0,\ \frac{\partial F_w}{\partial z} = 0 \qquad (4)$$

At $y = 0$:

$$\frac{\partial}{\partial y}\left(\frac{\partial^2 F}{\partial y^2} + \frac{\partial^2 F}{\partial z^2}\right) = 0,\ \frac{\partial F}{\partial y} = 0,\ \frac{\partial F_w}{\partial y} = 0 \qquad (5)$$

At $z = 1$:

$$\frac{\partial^2 F}{\partial y^2} + \frac{\partial^2 F}{\partial z^2} = 0,\ F = F_w,\ \frac{\partial F_w}{\partial z} = \left(\frac{\sigma_L}{\sigma}\right)\frac{\partial F}{\partial z} \qquad (6)$$

At $y = a$:

$$\left(\frac{\partial^2 F}{\partial y^2} + \frac{\partial^2 F}{\partial z^2}\right) = 0,\qquad \frac{\partial F}{\partial y} = \frac{\partial F_w}{\partial y}$$

$$\frac{\partial F_w}{\partial z} = \left(\frac{\sigma_H}{\sigma}\right)\frac{\partial F}{\partial z} \qquad (7)$$

At $z = 1 + d$:

$$F_w = 0 \qquad (8)$$

At $y = a + d$:

$$\frac{\partial F_w}{\partial y} = 0 \qquad (9)$$

3. THIN WALL APPROXIMATION, HARTMANN LAYER CONTRIBUTION TO THE FLUID ELECTRIC CURRENT AND LOAD RESISTANCE ATTACHMENT

(1)-(9) define the problem in terms of $F(y, z)$ and $F_w(y, z)$. To be in terms of a single variable, fluid and wall regions must be decoupled. That's the thin wall approximation: regarding $d \ll 1$ and the medium around the duct as isolating. Details on Rizzo-Sierra (2017). (7) results:

$$\frac{\partial F(a,z)}{\partial y} = \mathbb{C}_{\mathbb{H}} \frac{\partial^2 F(a,z)}{\partial z^2} \qquad (10)$$

(10) is valid within the thin wall approximation

$(M^{-1} \ll \mathbb{C}_{\mathbb{H}} \ll 1)$, but it needs modification since it does not give the correct limit when $\mathbb{C}_{\mathbb{H}} \to 0$ due to ignoring the discontinuity in j_y across the Hartmann layer. The electric current surface density z component is $j_z = u_c - \partial\phi/\partial z$ where $u_c = u_c (1 - e^{-M\xi})$ is the core-layer velocity profile as discussed in Moreau (1990). $\mathbb{C}_{\mathbb{H}} = d(\sigma_H/\sigma) = 0$ and $\mathbb{C}_{\mathbb{L}} = d(\sigma_L/\sigma) \to \infty$ are the Hartmann and side walls conductance ratios respectively, for the system to function as a generator. u_c is the core velocity and ξ is the coördinate perpendicular to the Hartmann wall measured from it. Due to ϕ continuity across the Hartmann layer, $\partial\phi/\partial z$ can be considered constant within an error of $O(M^{-2})$. Outside the layer, the electric current surface density z component is $j_{zC} = u_c - \partial\phi/\partial z$. The net current trough it is:

$$\int_0^\infty (j_z - j_{zC})d\xi = u_c \int_0^\infty e^{-M\xi}d\xi = \frac{u_c}{M} \qquad (11)$$

In terms of h, the fluid region electric current stream function is defined by $j_{yo} = -\partial h/\partial z$ and $j_{zo} = \partial h/\partial y$. (11) can be rewritten via (2):

$$\Delta h = M^{-1}\left(\frac{\partial^2 F(a,z)}{\partial y^2} + \frac{\partial^2 F(a,z)}{\partial z^2}\right) \qquad (12)$$

Adding to this last estimation the current into the load resistance (R_K) in (10) one gets:

$$\frac{\partial F(a,z)}{\partial y} - (\mathbb{C}_{\mathbb{H}} + M^{-1})\frac{\partial^2 F(a,z)}{\partial z^2} =$$
$$M^{-1}\frac{\partial^2 F(a,z)}{\partial y^2} + \frac{1}{R_k}\left(\frac{\partial F(a,1)}{\partial z}\right) - \qquad (13)$$
$$\frac{1}{R_k}\left(\frac{\partial F(a,0)}{\partial z}\right)$$

The last two terms in Eq. (13) come from Ohm's law. Since $\phi(y, z) = \partial F(y,z)/\partial z$, an estimate of the current through R_K (I_K) at $y = a$ is:

$$I_{K-0.25} = \frac{1}{2}\frac{\Delta\phi}{R_K} = \frac{1}{2}\frac{(2\Delta\phi')}{R_K} = \frac{\phi(a,z)\big|_{z=0}^{z=1}}{R_K} \qquad (14)$$

1/2 in (14) far left means that restricting the analysis to one of the Hartmann walls deals with one half of

the total through R_K. Factor of 2 in $2\Delta\phi'$ reflects 1/4 − 0.25 duct symmetry, as schematized in Fig. 3. One can notice that $\Delta\phi' = \Delta\phi/2$, once realizing that $\Delta\phi$ is the potential difference between side/lateral walls in Fig. 2. In dimensionless quantities:

$$\tilde{I}_{K-0.25} = \frac{\tilde{a}\Delta\tilde{\phi}}{\tilde{R}_K} = \frac{\tilde{a}\tilde{\phi}(\tilde{a},\tilde{z})\big|_{\tilde{z}=0}^{\tilde{z}=1}}{\tilde{R}_K} \qquad (15)$$

Non-dimensionalization equations used to obtain (15) were $\tilde{\Phi} = \Phi/u_0^* B_0 L$ for the electric potential, $\tilde{j} = j/\sigma u_0^* B_0$ for the electric current surface density, and $\tilde{R}_K = R_K/R_i$ for the load electric resistance. $R_i = b/\sigma al$ is an estimate for the generator internal electric resistance, l is the duct length and a, b half of the duct height and width respectively. Characteristic length used for non-dimensionalization was half of the duct width, i.e., $L = b = 1$. Since $\tilde{y} = y/L = y/b$, at $y = a$: $\tilde{y} = a/b = a/1 = \tilde{a}$. $\tilde{a}$ is then simultaneously half of the dimensionless duct height and its aspect ratio. On the other hand $\tilde{z} = z/b = z/1$. The non-dimensionalization relation resulting for the electric current is $\tilde{I} = I/\sigma u_0^* B_0 Ll = I/\sigma u_0^* B_0 bl = I/\sigma u_0^* B_0 l$.
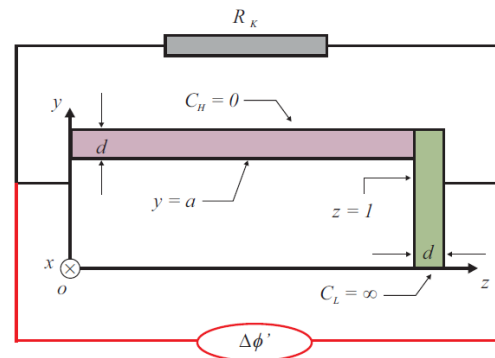

Fig. 3. Schematic of the generator setup taking into account 1/4 − 0.25 duct symmetry.

With (15), (1) to (9) result: a) Fluid region governing equation.

$$M^{-2}\left(\frac{\partial^2 u_0}{\partial y^2} + \frac{\partial^2 u_0}{\partial z^2}\right) - \frac{\partial^2 F}{\partial y^2} - iN_\omega^{-1}u_0 = G \qquad (16)$$

Where, given that $0 < y < a \land 0 < z < 1$:

$$u_0 = \frac{\partial^2 F}{\partial y^2} + \frac{\partial^2 F}{\partial z^2} \qquad (17)$$

b) Boundary conditions.

$$\frac{\partial}{\partial z}\left(\frac{\partial^2 F}{\partial y^2} + \frac{\partial^2 F}{\partial z^2}\right) = 0, \qquad \frac{\partial F}{\partial z} = 0 \qquad (18)$$

At $y = 0$:

$$\frac{\partial}{\partial y}\left(\frac{\partial^2 F}{\partial y^2}+\frac{\partial^2 F}{\partial z^2}\right)=0, \qquad \frac{\partial F}{\partial y}=0 \qquad (19)$$

At z = 1:

$$\left(\frac{\partial^2 F}{\partial y^2}+\frac{\partial^2 F}{\partial z^2}\right)=0, \qquad F+\mathbb{C}_L\frac{\partial F}{\partial z}=0 \qquad (20)$$

At y = a:

$$\left(\frac{\partial^2 F}{\partial y^2}+\frac{\partial^2 F}{\partial z^2}\right)=0,$$

$$\frac{\partial F}{\partial y}-\left(\mathbb{C}_H+M^{-1}\right)\frac{\partial^2 F}{\partial z^2}=M^{-1}\frac{\partial^2 F}{\partial y^2}+\frac{a}{R_K}\frac{\partial F}{\partial z}\Big|_{z=0}^{z=1} \qquad (21)$$

Last term in (21) bottom results from (13) considering (15) for $a \neq 1$. That is, (13) is correct for $a = 1$. Notice that $\partial F(a,0)/\partial z = 0$. In addition to conditions in (16) to (21), the formulation must also account the dimensionless volumetric flow conservation condition in terms of the averaged velocity amplitude (u_0):

$$\int_0^a \int_0^1 u_0 \, dydz = a \qquad (22)$$

(22) comes from $\int_{ds}\vec{u}_0 . \vec{ds}=\int_0^a\int_0^1 u_0 dydz=a$ since a is simultaneously the generator cross-section dimensionless area, half of its height, and aspect ratio. Because the spatial average of u_0 is

$$\langle u_0 \rangle = \frac{\int_{ds}\vec{u}_0.\vec{ds}}{\int_{ds}ds} \text{ , in order to normalize } u$$

respect to it:

$$u_n=\frac{u(x,y,z)}{\langle u_0 \rangle}=a\frac{u_0(y,z)e^{it}}{\int_0^a\int_0^1 u_0 dydz} \qquad (23)$$

4. NUMERICAL FORMULATION AND ISOTROPIC EFFICIENCY

To solve (16)-(21) with spectral collocation, a function $F = F(y,z)$ satisfying boundary conditions is proposed as a finite series of even Chebyshev polynomials ($T_{2m}(y/a)$, and $T_{2n}(z)$).

$$F=\sum_{m=0}^{N_y}\sum_{n=0}^{N_z}A_{mn}T_{2m}(\frac{y}{a})T_{2n}(z) \qquad (24)$$

Coefficients A_{mn} are to be determined. N_y and N_z are the number of terms to consider along y and z coördinates respectively. Use of Gauss-Lobatto collocation points set is advisable because it yields proper numerical resolution for the boundary layers by concentrating towards the walls. A_{mn} can be considered as a vector $\beta(AJ) = A_{mn}$, and the system of equations can be expressed as $\sum_{AJ=1}^{N_T}\alpha_{PJ\times AJ}\beta_{AJ}=\gamma_{PJ}$. $AJ = m(N_z + 1) + n + 1$,

$1 \le PJ \ \wedge \ AJ \le N_T$, and $N_T=(N_y+1)(N_z+1)$.

Elements of $\alpha_{PJ\times AJ}$ and known vector $\gamma_{(PJ)}$ are obtained by replacing (24) into (16)-(21). Explicitly, into (16):

$$\sum_{m=0}^{N_y}\sum_{n=0}^{N_z}\left(\begin{array}{l}\frac{1}{a^4}\frac{\partial^4 T_{2m}\left(\frac{y}{a}\right)}{\partial y^4}T_{2n}(z)+\frac{2}{a^2}\frac{\partial^2 T_{2m}\left(\frac{y}{a}\right)}{\partial y^2}\frac{\partial^2 T_{2n}(z)}{\partial z^2}\\ +T_{2m}\left(\frac{y}{a}\right)\frac{\partial^4 T_{2n}(z)}{\partial z^4}-\frac{M^2}{a^2}\frac{\partial^2 T_{2m}\left(\frac{y}{a}\right)}{\partial y^2}T_{2n}(z)\\ -i\frac{M^2 N_\omega^{-1}}{a^2}\frac{\partial^2 T_{2m}\left(\frac{y}{a}\right)}{\partial y^2}T_{2n}(z)\\ -iM^2 N_\omega^{-1}T_{2m}\left(\frac{y}{a}\right)\frac{\partial^2 T_{2n}(z)}{\partial z^2}\end{array}\right).A_{mm}=M^2 G$$

$$(25)$$

Replacing into (18) and (19), boundary conditions at $z = 0$ and $y = 0$ are identically satisfied, so no equations are generated. Into (20) left, the hydro-dynamic boundary condition at $z = 1$ results:

$$\sum_{m=0}^{N_y}\sum_{n=0}^{N_z}\left(\begin{array}{l}\frac{1}{a^2}\frac{\partial^2 T_{2m}\left(\frac{y}{a}\right)}{\partial y^2}\\ +\frac{4n^2}{3}\left(4n^2-1\right)T_{2m}\left(\frac{y}{a}\right)\end{array}\right).A_{mn}=0 \qquad (26)$$

Into (20) right, electromagnetic boundary condition at $z = 1$ results:

$$\sum_{m=0}^{N_y}\sum_{n=0}^{N_z}\left(T_{2m}\left(\frac{y}{a}\right)+4n^2\mathbb{C}_L T_{2m}\left(\frac{y}{a}\right)\right).A_{mn}=0 \quad (27)$$

Into (21) top, the hydrodynamic boundary condition at $y = a$ results:

$$\sum_{m=0}^{N_y}\sum_{n=0}^{N_z}\left(\frac{4m^2}{3a^2}\left(4m^2-1\right)+T_{2n}(z)\frac{\partial^2 T_{2n}(z)}{\partial^2 z}\right).A_{mn}=0 \qquad (28)$$

Into (21) bottom, the electromagnetic boundary condition at $y = a$ results:

$$\sum_{m=0}^{N_y}\sum_{n=0}^{N_z}\left(\begin{array}{l}\frac{4m^2}{a}T_{2n}(z)\\ -\left(\mathbb{C}_H+\frac{1}{M}\right)\frac{\partial^2 T_{2n}(z)}{\partial z^2}-\frac{4m^2 M^{-1}(4m^2-1)}{3a^2}T_{2n}(z)-\frac{4am^2}{R_K}\end{array}\right)A_{mn}=0 \qquad (29)$$

The linear system by (25)-(29) can be solved by any method. Then, the solution of (24) can be constructed. Alternatively, key to the characterization of a generator is its isotropic efficiency η_e, defined as the ratio between the system's time averaged output electric power $\langle P_e \rangle$ and its time averaged input power. The last is given by the power related to the oscillatory flow interacting with the electro-magnetic field $\langle P_f \rangle$ plus the time averaged power related to the system's heating by viscous dissipation $\langle P_\mu \rangle$,
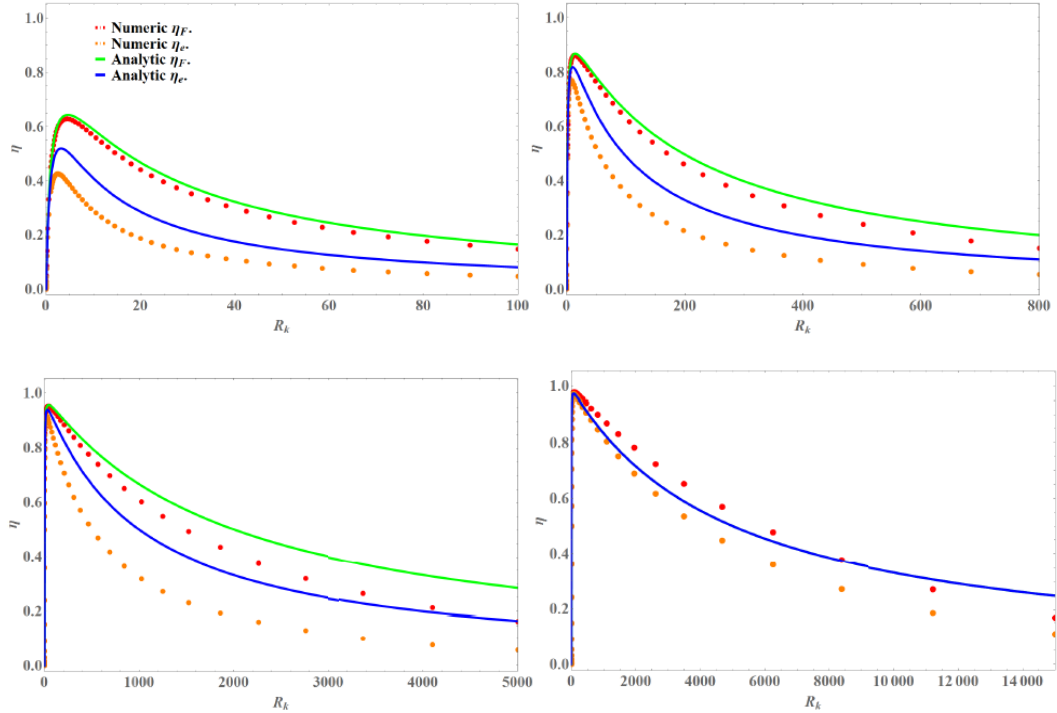
Fig. 4. 1 −D analytical vs. numerical generator's isotropic Faraday and electric efficiencies (η_F and η_e, respectively). $N_\omega = 10^6$, $a = 1$. Top left: $M = 10^1$. Top right: $M = 10^2$. Bottom left: $M = 10^3$. Bottom right: $M = 10^4$.

i. e., $\eta_e = \langle P_e \rangle \big/ \left(\langle P_f \rangle + \langle P_\mu \rangle \right)$.

$$\eta_e = \frac{\dfrac{1}{\tau} \int_0^\tau \int_V \vec{j} \cdot \vec{E} \, dVdt}{\dfrac{1}{\tau} \int_0^\tau \int_V \left(\vec{j} \times \vec{B} \right) \cdot \vec{u} dVdt + \dfrac{1}{\tau} \int_0^\tau \int_V \left(\mu \Phi_u \right) dVdt}$$

(30)

μ is the fluid's dynamic viscosity and $\mu\Phi_u$ its Newtonian viscous dissipation function, $\Phi_u = \left[\left(\partial u_x / \partial y \right)^2 + \left(\partial u_x / \partial z \right)^2 \right]$ Cf. Bird *et al.* (2002) $\langle \ \rangle$ denote time average integration over an integer number of periods (τ), and dV volumetric integration. There's also the Faraday's efficiency (without P_μ). To distinguish it from η_e we call it η_F. With the same non-dimensionalization factors used in the formulation, realizing that $\mu = \sigma B_0^2 L^2 \big/ M^2$. M is the Hartmann's number Rizzo-Sierra (2017) we have:

$$\tilde{\Phi}_\mu = \frac{1}{M^2} \left[\left(\frac{\partial \tilde{u}_x}{\partial \tilde{y}} \right)^2 + \left(\frac{\partial \tilde{u}_x}{\partial \tilde{z}} \right)^2 \right]$$

(31)

$\vec{j} \cdot \vec{E} \left(\left[Wm^{-3} \right] \right)$ is the electric power volumetric density for a conducting fluid interacting with the electromagnetic field, $\left(\vec{j} \times \vec{B} \right) \cdot \vec{u} \left(\left[Wm^{-3} \right] \right)$ is the flow power volumetric density due to the fluid's oscillatory motion (i.e., due to its mechanical

energy), and $\mu\Phi_u$ ($\left[Wm^{-3} \right]$) is the power volumetric density at which the fluid's mechanical energy is transformed into heat within the generator.

5. ANALYTICAL VS. NUMERICAL COMPARISON

In absence of experimental data, numerical calculations are validated if they are reasonably close to analytical results. In this paper that's not the objective due to the dissimilar nature of the models, as will be described. In this case an analytical solution is not viable. Hence, a comparison between an analytical one-dimensional (1−D) inductionless oscillatory solution against our numerical oscillatory solution on the isotropic efficiency in (30) is carried on. Analytical details on Appendix A. Figure 4 shows the comparison for a sample of the parametric range studied. Beyond the similarity on the curves in Fig. 4, is important to notice their common features. Numerical calculations show that $\eta_e > \eta_F$ in Fig. 4. Analytical calculations too, except in Fig. (4 bottom, right). That's expected since η_e considers viscous dissipation while η_F doesn't. Both imply that $\langle P_\mu \rangle \propto M^{-2}$. That's appreciated by looking at (31) for the numerical and (33) and (36) for the analytical one. Then, increasing M will progressively reflect $\eta_e \sim \eta_F$. This detail is appreciated from Fig. (4 top, left) up to Fig. (4 bottom, right), where the two analytical efficiencies are indistinguishable, while the numerical ones are as close as they get in the parametric range inquired. Increasing M also means prevalence of MHD effects due to higher intensity of

Table 1 *M/Nω* and *NY = NZ*, for the set of numerical experiments performed. *a* = 0.25, 0.5, 0.75, 1.0

$N_\omega \downarrow, M \rightarrow$	10^0	10^1	10^2	10^3	10^4
10^0	$10^0, 40$	$10^1, 40$	$10^2, 40$	$10^3, 70$	$10^4, 100$
10^1	$10^{-1}, 40$	$10, 40$	$10^1, 40$	$10^2, 70$	$10^3, 100$
10^2	$10^{-2}, 40$	$10^{-1}, 40$	$10^0, 40$	$10^1, 70$	$10^2, 100$
10^3	$10^{-3}, 40$	$10^{-2}, 40$	$10^{-1}, 40$	$10^0, 70$	$10^1, 100$
10^4	$10^{-4}, 40$	$10^{-3}, 40$	$10^{-2}, 40$	$10^{-1}, 70$	$10^0, 100$
10^5	$10^{-5}, 40$	$10^{-4}, 40$	$10^{-3}, 40$	$10^{-2}, 70$	$10^{-1}, 100$
10^6	$10^{-6}, 40$	$10^{-5}, 40$	$10^{-4}, 40$	$10^{-3}, 70$	$10^{-2}, 100$
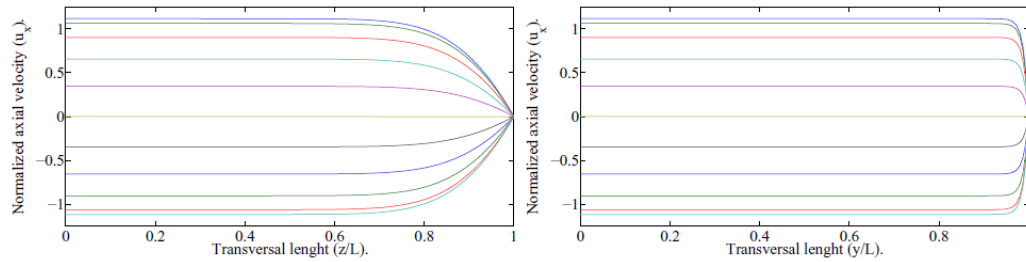
Fig. 5. Velocity profiles. $\mathbb{C}_\mathbb{H} = 0$, $\mathbb{C}_\mathbb{L} \rightarrow \infty$. $N_\omega = 10^5$, $M = 10^2$, $a = 1$; $M/N_\omega = 10^{-3}$. $R_K = 10^{-3}$. **Left image: profile at** $y = 0$. **Right image: profile at** $z = 0$.

the magnetic field. The treatment given by the analytical model on the electromagnetic conditions of the problem is less thorough than the numerical. Because it is $1 - D$, the analytical model does not develop a quantitative treatment on the electromagnetic boundary conditions defining the problem equally comparable to the numerical, summarized in sections 2, 3, and 4. Details on Rizzo-Sierra (2016). For example, while for the numerical model $\vec{E} = -\nabla\phi = \left[E_y(y,z)\hat{e}_y + E_z(y,z)\hat{e}_z\right]e^{it}$, for the 1 $-D$ analytical model $\vec{E} = -\nabla\phi = (E_0\hat{e}_z)e^{it}$, E_0 being a constant. This begins to explain why the two differ with increasing M values.

A formal validation between analytical and numerical models could not be our goal here, but a mutual cross-reference due to the disparity of their physical formulation due to the limitations of the analytical one. An analytical solution is not currently viable and there is no experimental data available on it neither, hence the need of numerical approaches. Successful validation instances of this basic numerical model before its application to the generator case (where analytical and numerical approaches were much more comparable) can be found in Rizzo-Sierra (2017), Rizzo-Sierra *et al.* (2016).

6. RESULTS

Once numerical results are comparable to analytical results, a generator characterization can be attempted. This is done by inquiring its behavior within a parametric range of interest. Parameters considered are the Hartmann number *M*, oscillatory interaction parameter N_ω, electric load resistance R_K,

and duct aspect ratio *a*. Emphasis was put on high Hartmann numbers because they characterize strong magnetic fields, favoring electric generation. N_ω range was chosen due to our interest in the flow at low frequencies having in mind LM-MHD generators. Collocation sets to obtain converging solutions are not such an issue in the LM-MHD generator situation as in the non generating flow discussed in Rizzo-Sierra (2017). There, interest revolved on velocity profiles and their correct side/lateral and Hartmann layers resolution, which require higher values for $NY \wedge NZ$ to obtain smoothed profiles towards the walls, mainly Hartmann's. Here, interest centers on $\langle P_e \rangle$, $\langle P_f \rangle$ and

$\langle P_\mu \rangle$ in order to obtain η_e in (30). The situation is grasped with Table 1, filled with values of *M/Nω*, *NY*, and *NZ*. The last two register values above which the numerical solution was stable up to three significant figures within the ranges checked for η_e and η_F. Figures 5 to 7 portrait velocity profiles over a semi-period $(0 - \pi \, Rads)$ in increments of $\pi/5 \, Rads$. They show how flow comply with characteristics similar to those described in Rizzo-Sierra (2017), with a new feature. Flow structure depends not only on increasing *M/Nω* ratio as shown in side wall figures (5 left), (6 left), (7 left); particularly on the last one. It also depends on R_K value, noticeable when comparing Figs. (5 left) and (7 left). Flow structure is the same but its distribution changes with R_K, as well as the surface electric current density distribution $\vec{j}$, as shown in Fig. 8, just to depict one example at $M/N_\omega = 10^{-3}$, where the trend is more perceivable. Notice also the higher phenomenological representativity of side wall layer
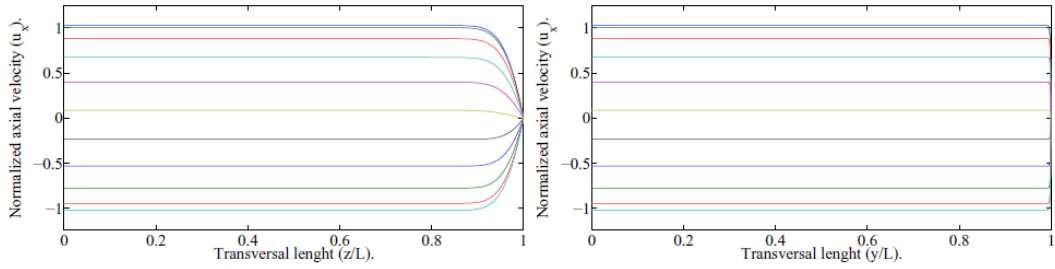
Fig. 6. Velocity profiles. $\mathbb{C}_{\mathbb{H}} = 0$, $\mathbb{C}_{\mathbb{L}} \to \infty$. $N_\omega = 10^4$, $M = 10^3$, $a = 1$; $M/N_\omega = 10^{-1}$. $R_K = 5000$. **Left image: profile at $y = 0$. Right image: profile at $z = 0$.**
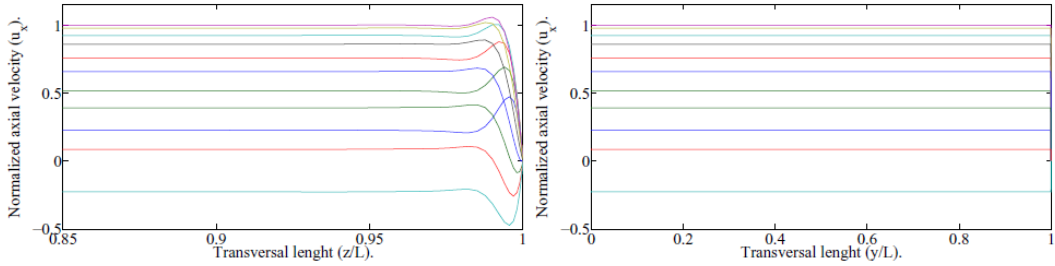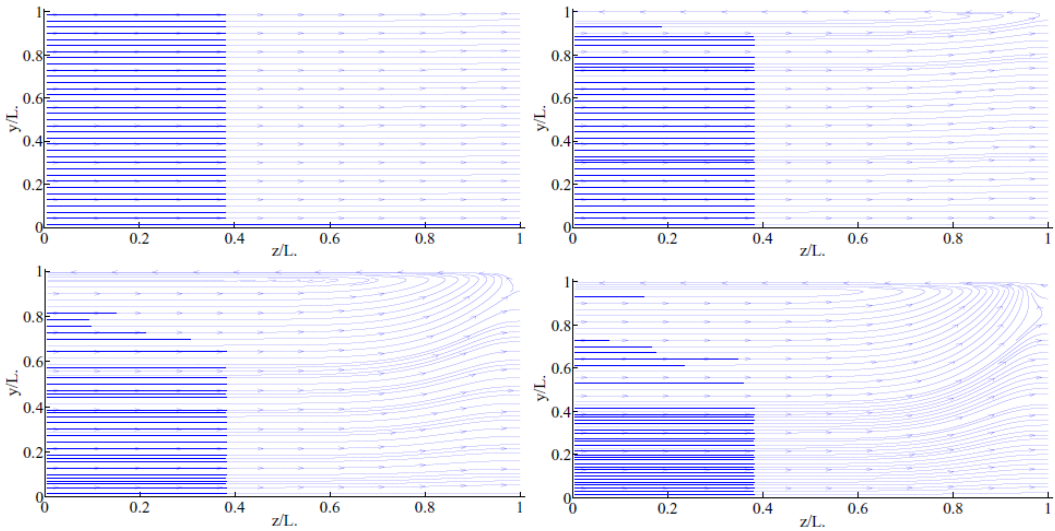

Fig. 7. Velocity profiles. $\mathbb{C}_{\mathbb{H}} = 0$, $\mathbb{C}_{\mathbb{L}} \to \infty$. $N_\omega = 10^3$, $M = 10^4$, $a = 1$; $M/N_\omega = 10^1$. $R_K = 15000$. **Left image: profile at $y = 0$. Right image: profile at $z = 0$.**

Fig. 8. $\vec{j}$ **distribution respect to M, N_ω, M/N_ω and R_K.** $N_\omega = 10^5$, $M = 10^2$, $a = 1$, $t = 0$ *Rads*; $M/N_\omega = 10^{-3}$. **Top left: $R_K = 10^{-3}$. Top right: $R_K = 10.3$. Bottom left: $R_K = 90.8$. Bottom right: $R_K = 800$.**

velocity profiles (left) over Hartmann's (right). Figures 9 to 12 illustrate the behavior of $\langle P_e \rangle$, $\langle P_f \rangle$, and $\langle P_\mu \rangle$ respect to M for a high N_ω in (9), (10) and a low N_ω in (11), (12). Notice that $\langle P_e \rangle$ maxima remain at the same level, trend consistent with different M values for $\langle P_e \rangle$. Explaining that is not straightforward since the parameters defining the problem (M, N_ω, and a) are embedded in the formulation. In (12), the amount of current inside the generator (j_G), not through the load resistance R_K, is

$j_G \propto M^{-1}$. Considering that $O(\vec{E}) \sim O(\vec{u} \times \vec{B})$ by means of Ohm's law, since $M = B_0 L \sqrt{\sigma/\rho \nu}$, it results that $O(\vec{E}) \propto M$. This means that $\langle P_e \rangle \propto M M^{-1}$, so the behavior of $\langle P_e \rangle$ respect to M seems reasonable. Notice how this is reflected in the $1 - D$ analytical model too by (34) combined with (33). For $\langle P_\mu \rangle$, it was discussed how $\langle P_\mu \rangle \propto M^{-2}$.

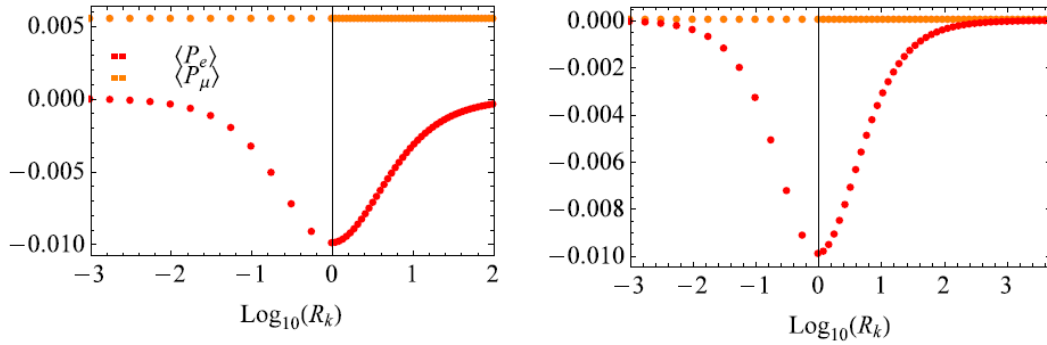This means viscous dissipation decreases rapidly with increasing M, which can be appreciated from

Fig. 9. $\langle P_e \rangle$ and $\langle P_\mu \rangle$ respect to M. $N_\omega = 10^6$, $a = 1$. Left: $M = 10^1$. Right: $M = 10^3$.
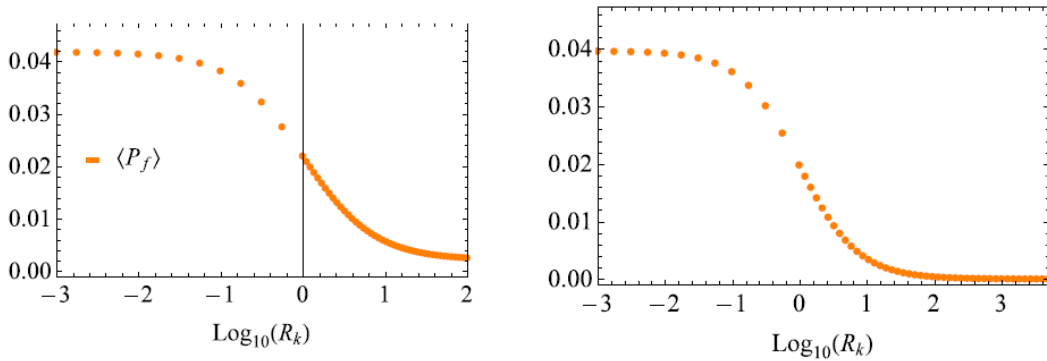

Fig. 10. $\langle P_f \rangle$ respect to M. $N_\omega = 10^6$, $a = 1$. Left: $M = 10^1$. Right: $M = 10^3$.
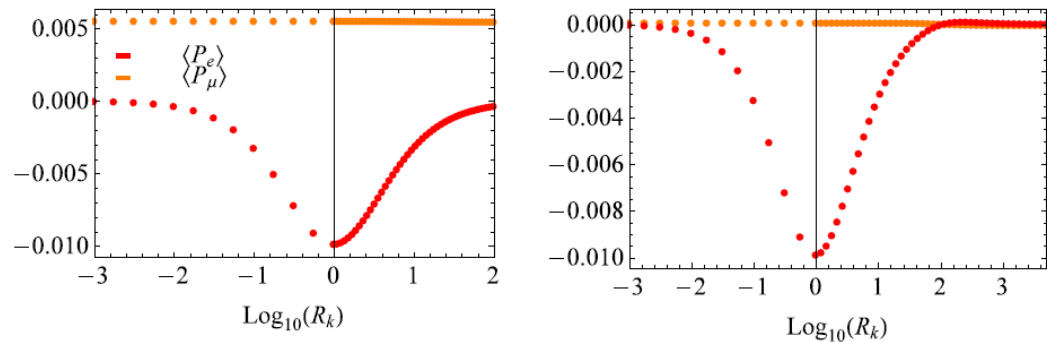

Fig. 11. $\langle P_e \rangle$ and $\langle P_\mu \rangle$ respect to M. $N_\omega = 10^2$, $a = 1$. Left: $M = 10^1$. Right: $M = 10^3$.

the figures. But $\langle P_\mu \rangle$ could also decrease with R_K, as noticeable in Fig. (11, right). Regarding that, (13) multiplied by M shows that the term related to the electric current through the load resistance R_K can then be considered $I_{K-0.25} \propto MR_K^{-1}$. Now, since $M^2 = N_\omega R_\omega$, $M \propto \sqrt{N_\omega} \Leftrightarrow N_\omega \propto M^2$. Therefore, $I_{K-0.25} \propto \sqrt{N_\omega} R_K^{-1}$. This means that for low interaction parameters such as $N_\omega = 10^2$, less current is drawn from the generator for a fixed R_K, which translates into stronger Lorentz forces acting on the fluid proportional to $\vec{j} \times \vec{B}$, and therefore into greater averaged velocity gradients in (31), leading to greater $\langle P_\mu \rangle$ values diminishing with increasing R_K values. By the way, it must be noticed that

$\langle P_f \rangle \propto \vec{j} \times \vec{B}$ as well. The difference with the situation depicted in Fig. (9, right) is that at $N_\omega = 10^6$, more current is drawn from the generator for a fixed R_K, so the averaged velocity gradients in (31) result smaller and the effect described is damped. Since $\langle P_f \rangle \propto \vec{j} \times \vec{B}$, by similar considerations to the ones just used for $\langle P_e \rangle$, $\langle P_f \rangle \propto MM^{-1}$. This way, what is shown in Figs. 10 and 12 seems reasonable as well. Figures 13 to 16 inquire the influence of N_ω on $\langle P_e \rangle$, $\langle P_f \rangle$ and $\langle P_\mu \rangle$. For the latter, since $\langle P_\mu \rangle \propto M^{-2}$, it is clear why $\langle P_\mu \rangle$ is higher for M^2 in Fig. 13 than for M^4 in Fig. (15).
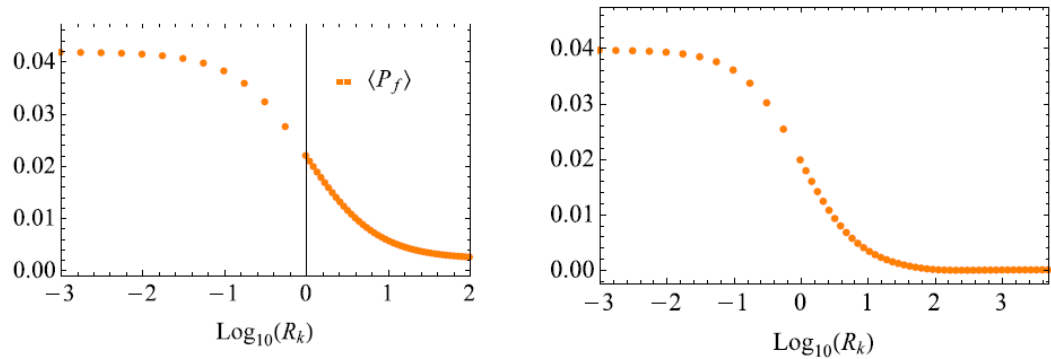
Fig. 12. $\langle P_f \rangle$ respect to M. $N_\omega = 10^2$, $a = 1$. Left: $M = 10^1$. Right: $M = 10^3$.
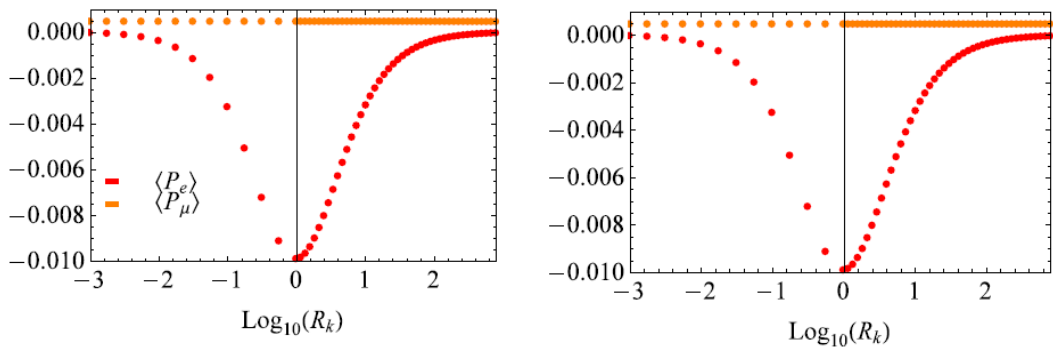

Fig. 13. $\langle P_e \rangle$ and $\langle P_\mu \rangle$ respect to N_ω. $M = 10^2$, $a = 1$. Left: $N_\omega = 10^3$. Right: $N_\omega = 10^6$.
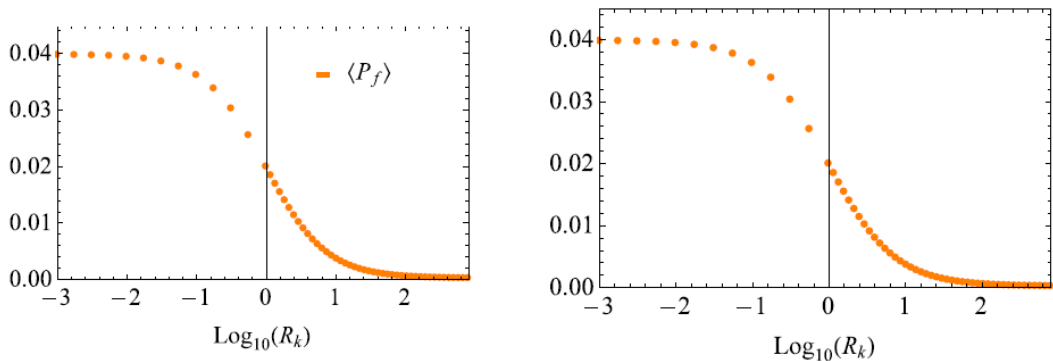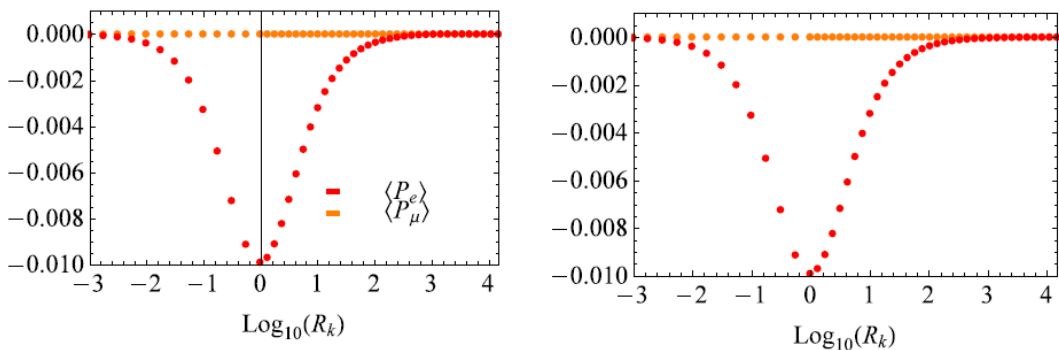

Fig. 14. $\langle P_f \rangle$ respect to N_ω. $M = 10^2$, $a = 1$. Left: $N_\omega = 10^3$. Right: $N_\omega = 10^6$.

Fig. 15. $\langle P_e \rangle$ and $\langle P_\mu \rangle$ respect to N_ω. $M = 10^4$, $a = 1$. Left: $N_\omega = 10^3$. Right: $N_\omega = 10^6$.

Remembering Fig. (11, right), when the situation is checked for $M = 10^3$ and $N_\omega = 10^2$ (not shown here), an analogue occurrence is found, so the same considerations apply regarding $\langle P_\mu \rangle$ respect to N_ω.

Moreover, no apparent effect of N_ω on $\langle P_e \rangle$ for this parametric range is observed. Focusing on that, it was previously stated that $\langle P_e \rangle \propto MM^{-1}$. Recalling
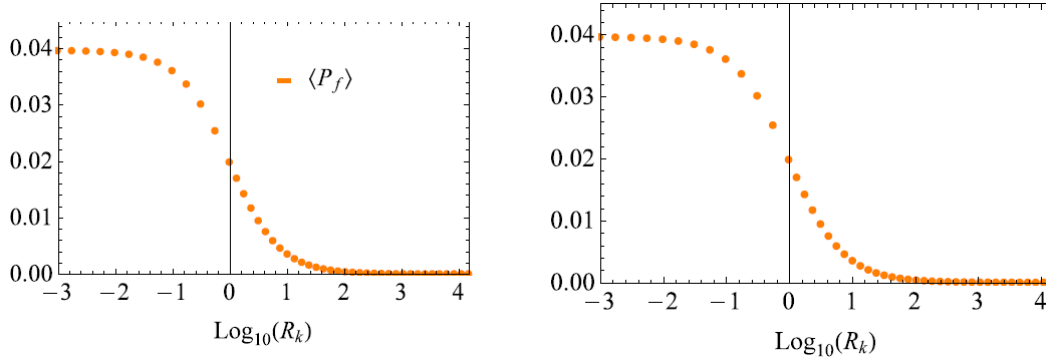
Fig. 16. $\langle P_f \rangle$ **respect to** N_ω. $M = 10^4$, $a = 1$. **Left:** $N_\omega = 10^3$. **Right:** $N_\omega = 10^6$.
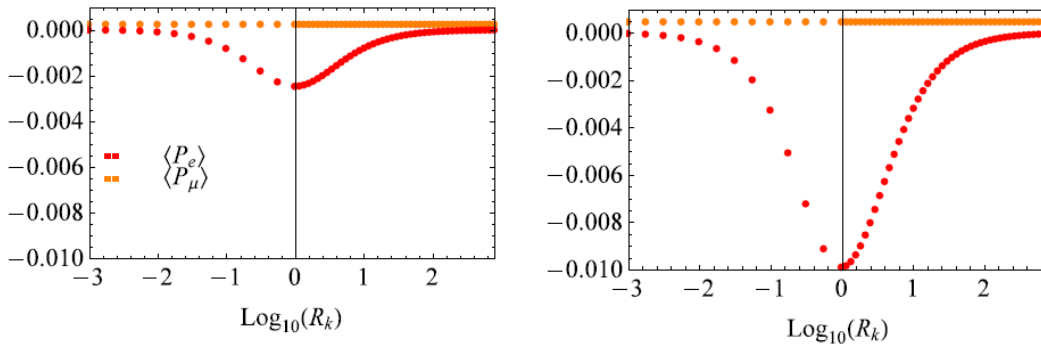

Fig. 17. $\langle P_e \rangle$ **and** $\langle P_\mu \rangle$ **respect to** a. $M = 10^2$, $N_\omega = 10^4$. **Left:** $a = 0.25$. **Right:** $a = 1$.
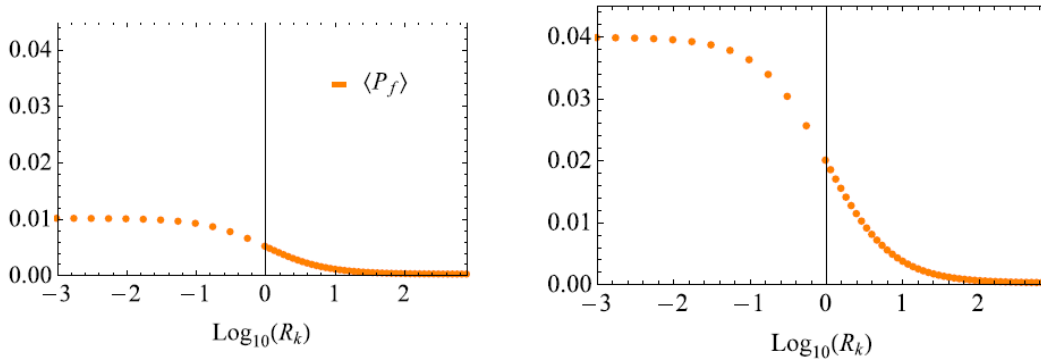

Fig. 18. $\langle P_f \rangle$ **respect to** a. $M = 10^2$, $N_\omega = 10^4$. **Left:** $a = 0.25$. **Right:** a=1.
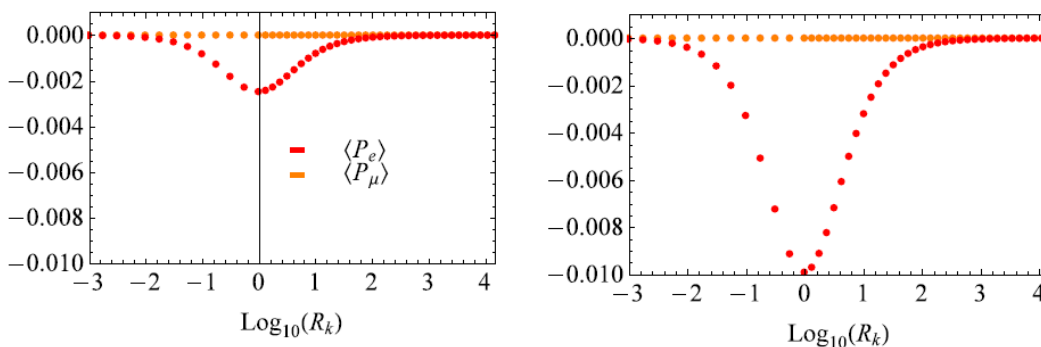

Fig. 19. $\langle P_e \rangle$ **and** $\langle P_\mu \rangle$ **respect to** a. $M = 10^4$, $N_\omega = 10^4$. **Left:** $a = 0.25$. **Right:** $a = 1$.

that $M^2 = N_\omega R_\omega$, $M \propto \sqrt{N_\omega} \Leftrightarrow N_\omega \propto M^2$. This way we can rewrite $\langle P_e \rangle \propto N_\omega^{1/2} N_\omega^{1/2}$, so the behavior of $\langle P_e \rangle$ respect to N_ω seems reasonable as well. Analogue considerations conduce to $\langle P_f \rangle \propto N_\omega^{1/2} N_\omega^{1/2}$, so Figs. 13 and 16 do not surprise. In their part, Figs. 17 to 20 inquire the influence of the aspect ratio a on $\langle P_e \rangle$,
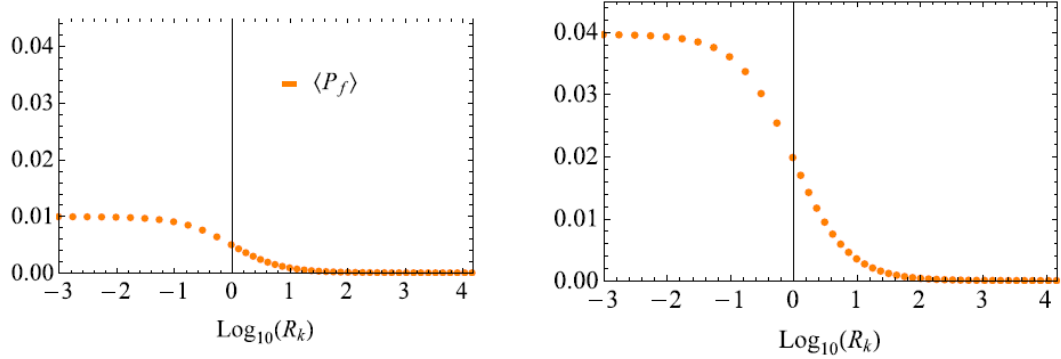
Fig. 20. $\langle P_f \rangle$ respect to a. $M = 10^4$, $N_\omega = 10^4$. **Left:** $a = 0.25$. **Right:** a=1.

Fig. 21. $\langle \eta_e \rangle$ and $\langle \eta_F \rangle$ respect to M. $N_\omega = 10^6$, $a = 1$. **Left:** $M = 10^1$. **Right:** $M = 10^4$.
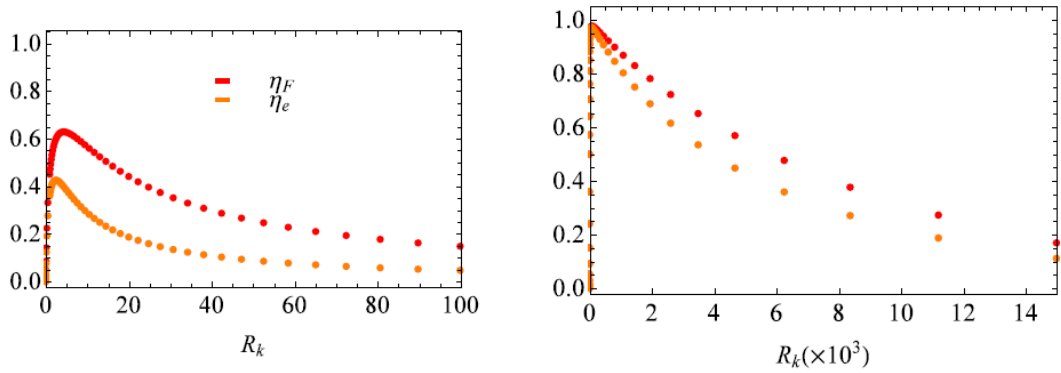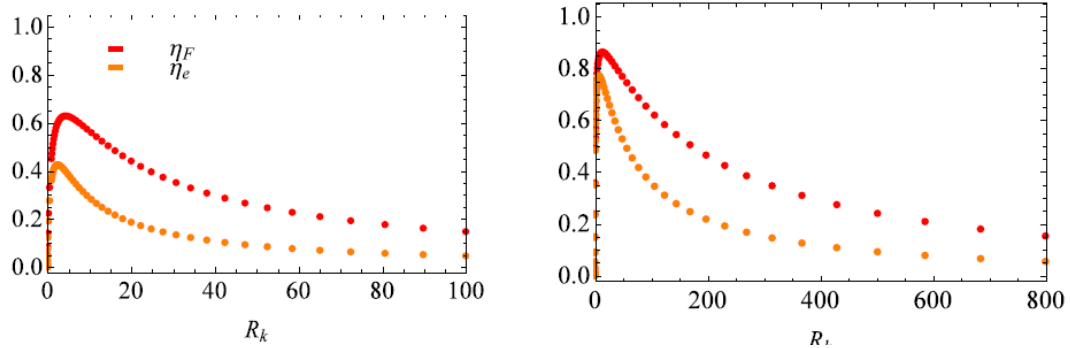

Fig. 22. $\langle \eta_e \rangle$ and $\langle \eta_F \rangle$ respect to M. $N_\omega = 10^2$, $a = 1$. **Left:** $M = 10^1$. **Right:** $M = 10^2$.

$\langle P_f \rangle$ and $\langle P_\mu \rangle$. No appreciable effects are detected for $\langle P_\mu \rangle$ over this parametric range since $O(\langle P_\mu \rangle) \sim M^{-2} \sim 0$ for increasing M. The situation for $\langle P_e \rangle$ and $\langle P_f \rangle$ is as one should expect for a rectangular cross-sectioned duct, since $\langle P_e \rangle = \frac{1}{\tau} \int_0^\tau \int_0^l \int_0^1 \int_0^a (\vec{\jmath} \cdot \vec{E}) \, dz dy dx dt$, $\langle P_f \rangle = \frac{1}{\tau} \int_0^\tau \int_0^l \int_0^1 \int_0^a [(\vec{\jmath} \times \vec{B}) \cdot \vec{u}] \, dz dy dx dt$ That is, in principle $\langle P_e \rangle \propto aMM^{-1}$ and $\langle P_f \rangle \propto aMM^{-1}$ if one were to consider $\partial/\partial y (\vec{\jmath} \cdot \vec{E}) \wedge \partial/\partial z (\vec{\jmath} \cdot \vec{E}) \sim 0$ and $\partial/\partial y [(\vec{\jmath} \times \vec{B}) \cdot \vec{u}] \wedge \partial/\partial z [(\vec{\jmath} \times \vec{B}) \cdot \vec{u}] \sim 0$ or what would happen with variations of terms $\vec{\jmath} \cdot \vec{E}$ and $(\vec{\jmath} \times \vec{B}) \cdot \vec{u}$ for fixed M. The smaller the aspect ratio, the smaller the induced current, and so the smaller $\langle P_e \rangle$ or $\langle P_f \rangle$. $\langle \eta_e \rangle$ and $\langle \eta_F \rangle$ behavior respect to M is shown in Fig. 21 for a high oscillatory interaction parameter and Fig. 22 for a lower one. The influence of M respect to $\langle \eta_e \rangle$ and $\langle \eta_F \rangle$ is clear. To explain it, previous arguments can be employed again. It was discussed how the current density flowing inside the generator is $j_G \propto M^{-1}$, and that current through R_k is $I_{K-0.25} \propto MR_K^{-1}$. Thus, for a fixed R_k an increment in M would translate into less current flowing inside the generator and simultaneously more current drawn from it. Both effects compensate for a fixed R_k when considering the order of $\langle P_e \rangle$, but regarding $\langle P_f \rangle$, in principle more current drawn from the generator means less Lorentz force acting on the
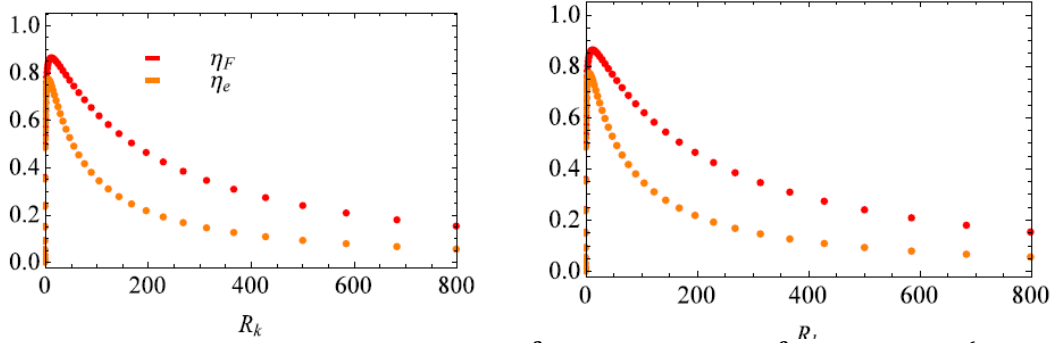
Fig. 23. $\langle\eta_e\rangle$ and $\langle\eta_F\rangle$ respect to N_ω. $M = 10^2$, $a = 1$. Left: $N_\omega = 10^3$. Right: $N_\omega = 10^6$.
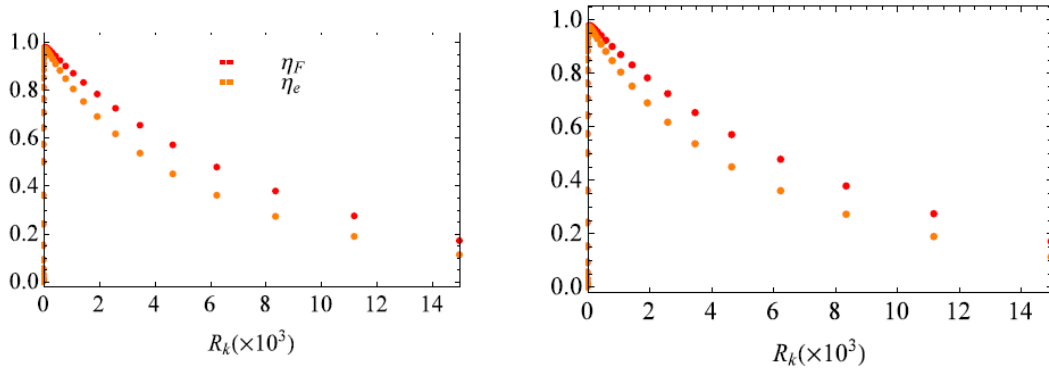

Fig. 24. $\langle\eta_e\rangle$ and $\langle\eta_F\rangle$ respect to N_ω. $M = 10^4$, $a = 1$. Left: $N_\omega = 10^3$. Right: $N_\omega = 10^4$.

fluid and therefore decreasing $\langle P_f\rangle$ values since $\langle P_f\rangle \propto \vec{j} \times \vec{B}$. This explains why $\langle\eta_e\rangle$ and $\langle\eta_F\rangle$ keep increasing with increasing M. There's no apparent effect from the part of N_ω for the parametric range presented, as occurred with $\langle P_\mu\rangle$. Figures 23 and 24 illustrate the behavior of $\langle\eta_e\rangle$ and $\langle\eta_F\rangle$ respect to N_ω. As previously discussed, there's no explicit intervention of N_ω in (30), which defines $\langle\eta_e\rangle$ and $\langle\eta_F\rangle$, but the same arguments employed keep applying. If $\langle P_e\rangle \propto N_\omega^{1/2}N_\omega^{-1/2}$, $\langle P_F\rangle \propto MM^{-1} \propto N_\omega^{1/2}N_\omega^{-1/2}$; and that's reflected in the analytical model as well by (35) and (33) combined. Furthermore, since $\langle P_\mu\rangle \propto N_\omega^{-1}$, it is clear that $\langle\eta_e\rangle$ and $\langle\eta_F\rangle$ will vary very slowly if any at all with respect to that specific parameter, and that's precisely noticed in those figures. Change respect to M is clear though. In their turn, Figs. 25 and 26 show $\langle\eta_e\rangle$ and $\langle\eta_F\rangle$ respect to a. Observations analogue to the ones previously discussed wrap up these comments. Since $\langle P_e\rangle \propto aMM^{-1}$ and $O(\langle P_\mu\rangle) \sim M^{-2} \sim 0$, the behavior of $\langle\eta_e\rangle$ and $\langle\eta_F\rangle$ in those figures is reasonable with increasing a and M. In summary, a brief illustration on the flow ($\vec{u}$) and surface electric current density distribution ($\vec{j}$) in the generator is carried on with Figs. 5 to 8. Parameters concerning generator performance are M, N_ω, and a through $\langle P_e\rangle$, $\langle P_f\rangle$, $\langle P_\mu\rangle$ and features of η_e and η_F were investigated as follows: varying number of collocation points (*NY* and *NZ*), not shown here; $\langle P_e\rangle$, $\langle P_f\rangle$, and $\langle P_\mu\rangle$ respect

to M, see Figs. 9 to 12; $\langle P_e\rangle$, $\langle P_f\rangle$, and $\langle P_\mu\rangle$ respect to a, see Figs. 17 to 20; η_e and η_F respect to M, see Figs. 32 to 22; η_e and η_F respect to N_ω, see Figs. 23 and 24; η_e and η_F respect to a, see Figs. 25 and 26. As a side result outside our scope, we can estimate dimensions and operation ranges of prospective LM-MHD generators. We can use $\langle P_e\rangle = (\sigma u_0^{*2}B_0^2 L^3)\langle\tilde{P}_e\rangle = (\rho\nu u_0^{*2}M^2 L)\langle\tilde{P}_e\rangle = (\rho\omega N_\omega u_0^{*2}L^3)\langle\tilde{P}_e\rangle$, obtained from previous expression. Figures 9, 11, 13, 15, 17, and 19 show how for $a = 1$, $O(|\langle\tilde{P}_e\rangle|) \sim 10^{-2}$ as a peak value. With fluids such as Hg, Na, $Ga^{68}In^{20}Sn^{12}$, $Na^{22}K^{78}$, $PbLi^{17}$ with $10^5 \lesssim O(\sigma) \lesssim 10^6 A/V.m$, magnetic fields of $O(B_0) \lesssim 10^0 T$, generator semi widths b of $O(b = L) \sim 10^{-1}$ (L being the motion's characteristic length), and motion's characteristic velocities of $O(u_0^*) \sim 10^1 m/s$, we obtain that a mesoscale generator having in mind "household" devices can reach dimensional peak averaged output powers of $O(|\langle P_e\rangle|) \lesssim 10^3 W$. That translates into *peak* averaged volumetric power densities (ρ_E) of $O(\rho_E) \lesssim 10^5 W/m^3$ when considering axial longitudes of $O(l) \sim 10^0 m$. This means they can produce *peak* dimensional averaged output powers of $O \lesssim 10^3 W$ for domestic energy consumption (corresponding to $\lesssim 8760 kW.h/year$), being of $O \lesssim 10^{-2} m^3$, at $0.05 \lesssim \eta_e \lesssim 0.9$ for Hg ($M \sim 10^3$) and Na ($M \sim 10^3$); or $0.1 \lesssim \eta_e \lesssim 0.95$ for $PbLi^{17}$ ($M \sim 10^4$), $Ga^{68}In^{20}Sn^{12}$ ($M \sim 10^4$) and $Na^{22}K^{78}$ ($M \sim 10^4$) depending on R_K. Figs. 21-26.
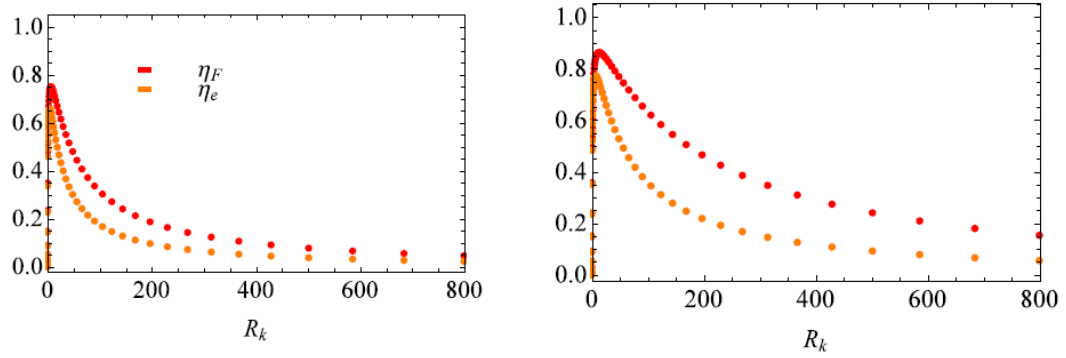
Fig. 25. $\langle \eta_e \rangle$ and $\langle \eta_F \rangle$ respect to a. $M = 10^2$, $N_\omega = 10^2$. **Left:** $a = 0.25$. **Right:** $a = 1$.
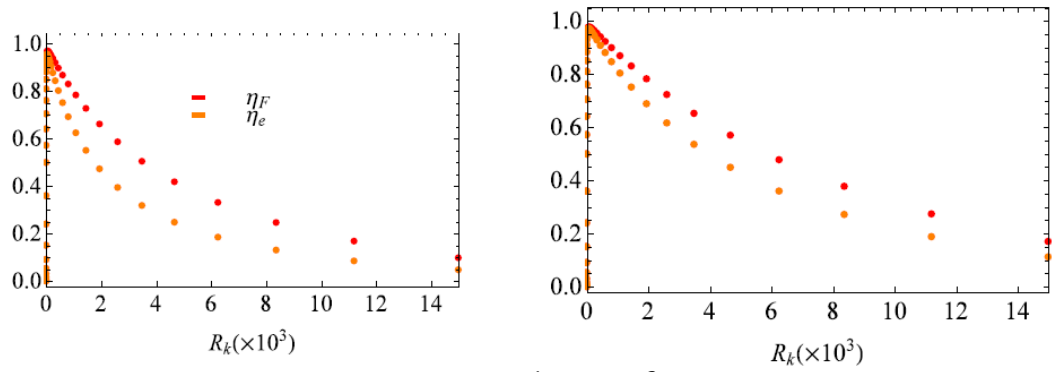

Fig. 26. $\langle \eta_e \rangle$ and $\langle \eta_F \rangle$ respect to a. $M = 10^4$, $N_\omega = 10^2$. **Left:** $a = 0.25$. **Right:** $a = 1$.
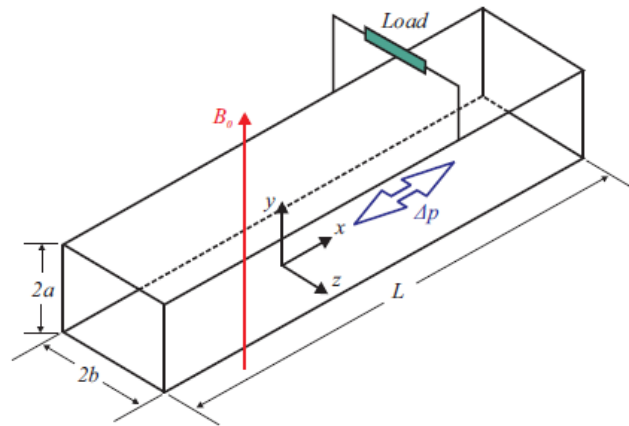

Fig. 27. Layout of the problem & its basic scheme.

Table 2 Generator's dimensional averaged power output estimates in order of magnitude for different liquid metals as working fluids. Externally applied magnetic fields of $O(B_0) \sim 10^0\ T$, characteristic lengths of $O(L) \sim 10^{-1}\ m$ (i.e., cross-sections of $O \sim 10^{-2}\ m^2$), axial longitudes of $O(l) \sim 10^0\ m$, $a = 1$.

Liquid metal	$O(M)$	$O(N_\omega)$	$O(u_0^\star)\ [m \cdot s^{-1}]$	$O(\omega)\ [s^{-1}]$	$O(|\langle P_e \rangle|)\ [W]$	$O(\rho_E)\ [W \cdot m^{-3}]$	$\eta_e\ (\times 10^{-2})$
Na	10^3	10^3	10^1	10^1	10^3	10^5	$5 \lesssim \eta_e \lesssim 90$
Hg	10^3	10^3	10^1	10^{-1}	10^3	10^5	$5 \lesssim \eta_e \lesssim 90$
$Ga^{68}In^{20}Sn^{12}$	10^4	10^3	10^1	10^0	10^3	10^5	$10 \lesssim \eta_e \lesssim 95$
$Na^{22}K^{78}$	10^4	10^3	10^1	10^1	10^3	10^5	$10 \lesssim \eta_e \lesssim 95$
$PbLi^{17}$	10^4	10^3	10^1	10^0	10^3	10^5	$10 \lesssim \eta_e \lesssim 95$

According to Yohanis *et al.* (2008), the 2005 average household energy consumption (E_H) in the UK was $2000 \lesssim E_H \lesssim 12000 \; kW.h/year$. Calculations in Table 2 comply with $R_m = \mu_B \sigma u_0^* L \sim \mu_0 \sigma u_0^* L \ll 1$. u_0^* is any velocity characteristic to the motion. $u_0^* = \Re\left[\frac{1}{\tau}\int_0^\tau \left(\int_{ds} \vec{u}_0.\vec{ds} \Big/ \int_{ds} ds\right) e^{it} dt\right]$ is the period average of the fluid velocity amplitude spatial average as introduced in (22), (23). Since $u(y,z) = \Re\left[u_0(y,z)e^{it}\right]$, $u_0^* \sim 0$. In the limit of u_0^* taken as a fraction in the definition of R_m, one has $R_m \ll 1$. Future work: first, a detailed study on the rescaling is required to determine dimensions of a prototype potentially useful in experimental protocols. Then, a comparison of numerical and experimental figures could ascertain both physical/numerical and experimental shortcomings. For example, temperature dependence of the values used to obtain Table 2 was not considered since they were given in orders of magnitude and its variation over valid temperature ranges is not significant, Cf. Müller *et al.* (2001). Finer estimates can use polynomial fitting (i.e., $\sigma = \sigma(T)$, and $\nu = \nu(T)$). Beyond the scope of this paper, analyses studying the overall influence of temperature on the generator operation can and must be developed as well.

7. CONCLUSION

The performance characterization of a generator was conducted by calculating its isotropic electric efficiency. The model consisted of a harmonically driven liquid metal fully developed incompressible viscous laminar oscillatory flow confined to a rectangular channel interacting with a uniform magnetic field and attached to a load resistance. Spectral collocation method was used to solve the boundary-conditioned Navier-Stokes equation under *inductionless* approximation for the magnetic field with implementation of gradient formulation for the electric field. Numerical calculations were compared with a $1 - D$ analytical solution developed for the same problem, finding reasonable agreement. Performance characterization is done in terms of dimensionless parameters defining the problem: M, N_ω, and a. Influence on η_e and η_F of these parameters through $<P_e>$, $<P_f>$ and $<P_\mu>$ was investigated as well.

APPENDIX A. ANALYTICAL EXPRESSIONS

Schematics in Fig. 27. It is a $(1 - D)$ analytical model for a LM-MHD closed rectangular channel alternate generator. The model was developed by Dr. Raúl Alejandro Ávalos Zúñiga and Gabriel García at CICATA-IPN, Santiago de Querétaro, Querétaro, México (Cf. Rizzo-Sierra (2016)). Using $\tilde{u}_0 = u_0/U$, $\tilde{G}_0 = G_0/Ua^{-2}\rho\nu$, $N_\omega = \sigma B_0^2/\rho\omega$, $\tilde{R}_K = R_K/R_i$, and $\chi = y/a$, the quantities needed to calculate η_e in (30) are obtained. That is, $<P_e>$, $<P_f>$ and $<P_\mu>$. U is a characteristic velocity for the system, u_0 is the velocity field amplitude, G_0 is the pressure gradient amplitude, $R_i = b/\sigma al$ is an estimate of the system's internal resistance. With:

$$f_0(\chi) = 1 - \frac{\cosh\left(M\sqrt{1+iN_\omega^{-1}\chi}\right)}{\cosh\left(M\sqrt{1+iN_\omega^{-1}}\right)} \qquad (32)$$

$$\tilde{u}_0(\chi) = \frac{\tilde{G}_0}{M^2\left(iN_\omega^{-1}+\left(1-\langle f_0\rangle K_0\right)\right)} f_0(\chi) \qquad (33)$$

one can obtain:

$$\left\langle \tilde{P}_e \right\rangle = 2M^2\left(1-K_0\right)K_0\langle\tilde{u}_0(\chi)\rangle\overline{\langle\tilde{u}_0(\chi)\rangle} \qquad (34)$$

$$\left\langle \tilde{P}_f \right\rangle = 2M^2\left(\left\langle\widetilde{u_0(\chi)\overline{u_0(\chi)}}\right\rangle - K_0\langle\tilde{u}_0(\chi)\rangle\overline{\langle\tilde{u}_0(\chi)\rangle}\right) \qquad (35)$$

$$\left\langle \tilde{P}_\mu \right\rangle = 2\left\langle\frac{\partial\tilde{u}_0(\chi)}{\partial\chi}\frac{\overline{\partial\tilde{u}_0(\chi)}}{\partial\chi}\right\rangle \qquad (36)$$

Tildes indicate dimensionless quantities, and one bar above signifies taking a quantity's complex conjugate. Non-dimensionalization equations result: $\left\langle\tilde{P}_e\right\rangle = \left\langle P_e\right\rangle a/bL\rho\nu U^2$, $\left\langle\tilde{P}_f\right\rangle = \left\langle P_f\right\rangle a/bL\rho\nu U^2$, $\left\langle\tilde{P}_\mu\right\rangle = \left\langle P_\mu\right\rangle a/bL\rho\nu U^2$. $K_0 = R_k/R_i + R_k = 1/1 + \tilde{R}_K^{-1}$, (dimensionless by definition) is the load factor for the system considered also as $K_0 = -E_0/\langle u_0\rangle B_0$. E_0 is the electric field amplitude across the load resistance, and as before, B_0 is the externally applied magnetic field.

REFERENCES

Bird, R. B., W. E. Stewart and E. N. Lightfoot (2002). *Transport phenomena*. John Wiley & Sons, New York.

Cuevas, S. (1994). *Liquid-metal flow and heat transfer under strong magnetic fields*. Ph. D. thesis. Facultad de Ciencias, Universidad Nacional Autónoma de México,

Cuevas, S., B. F. Picologlou, J. S. Walker and G. Talmage (1997). Liquid-metal MHD flow in rectangular ducts with thin conducting or insulating walls: laminar and turbulent solutions. International *Journal of Engineering Science* 35(5), 485-503.

Danilyan, A. V., D. L. Dorofeev, V. I. Naski-dashvili, G. V. Pakhomov and B. A. Zon (2005). Magnetohydrodynamic generator of pseudosound. *Acoustical Physics* 51(5), 598-600.

Davidson, P. A. (2001). *An Introduction to Magnetohydrodynamics*. Cambridge Univ. Press.

Hu, L., H. Kobayashi and Y. Okuno (2015). Analyses on response of a liquid metal MHD power generation system to various external inputs. *IEEJ Transactions on Electrical and*

Electronic Engineering 10(3), 268-273.

Ibáñez, G., S. Cuevas, and M. L. de Haro (2002). Optimization analysis of an alternate magnetohydrodynamic generator. *Energy Conversion and Management* 43(14), 1757-1771.

Intani, P., T. Sasaki, T. Kikuchi and N. Harada (2010). Analysis of disk AC MHD generator performance by finite element method. *Journal of Plasma Fusion Research (Japan)* 9, 580–585.

Ishikawa, M., K. Tamai, J. Umoto and V. A. Bityurin (1996). Three-dimensional analysis of near-electrode phenomena of Faraday type MHD generator. *In Proceedings of 12th International Conference on MHD*, Volume 2, pp. 886-895.

Jackson, W. D. (1963). Liquid-Metal Faraday-Type MHD Generators. Power, *IEEE Transactions on Apparatus and Systems* 82(69), 904-907.

Kobayashi, H., H. Shionoya and Y. Okuno (2011). Influence of non-uniform magnetic flux density on turbulent MHD flows in a liquid metal MHD power generator. *In 42nd AIAA Plasmadynamics and Lasers Conference*, Volume N. A., pp. 1–4.

Koslover, R. A. and R. C. Law (2007, January 23). Modular liquid-metal magneto-hydrodynamic (LMMHD) power generation cell. US Patent 7,166,927.

Liu, B., J. Li, Y. Peng, L. Zhao, R. Li, Q. Xia and C. Sha (2014). Performance study of magnetohydrodynamic generator for wave energy. In *The Twenty-fourth International Ocean and Polar Engineering Conference*. International Society of Offshore and Polar Engineers.

Liu, B., Y. Peng, L. Zhao, J. Li, R. Li, Y. Xu and C. Sha (2011). Hydrodynamic modelling of heaving buoy wave energy conversion system with liquid metal magnetohydrodynamic generator. In *Proceedings of the Twenty-first International Offshore and Polar Engineering Conference,* pp. 695–700.

Müller, U. and L. Bühler (2001). *Magnetofluiddynamics in channels and containers*. Springer Verlag.

Migliori, A. and G. Swift (1988). Liquid-sodium thermoacoustic engine. *Applied Physics Letters* 53(5), 355-357.

Moreau, R. J. (1990). *Magnetohydrodynamics*. Springer Science & Business Media.

Niu, X. D., H. Yamaguchi, X. J. Ye and Y. Iwamoto (2014). Characteristics of a MHD power generator using a low-melting-point Gallium alloy. *Electrical Engineering* 96(1), 37-43.

Nomura, O. (1988). A new method for the three-dimensional analysis of MHD generator channel. *Electrical Engineering in Japan* 108(5), 67-74.

Rizzo-Sierra, J. A. (2017). Numerical study on the magnetohydrodynamics of a liquid metal oscillatory flow under inductionless approximation. *Journal of Applied Fluid Mechanics* 10(1), 459-477.

Rizzo-Sierra, J. A. (Centro de Investigación en Ciencia Aplicada y Tecnología Avanzada, Instituto Politécnico Nacional, CICATA-IPN, 2016). *Characterization of a liquid metal magnetohydrodynamic generator under inductionless approximation*. Ph. D. thesis.

Rizzo-Sierra, J. A. and O. I. López-Hernández (2016). Numerical study on the magnetohydrodynamics of an oscillatory flow under inductionless and core-side-layer approximations. *Revista Mexicana de Física* 62(4), 369-380.

Satyamurthy, P., N. Venkatramani, A. M. Quraishi and A. Mushtaq (1999). Basic design of a prototype liquid metal magnetohy-drodynamic power generator for solar and waste heat. *Energy Conversion and Management* 40(9), 913-935.

Shionoya, H., H. Kobayashi and Y. Okuno (2011). Numerical study on turbulent flows in a liquid metal MHD generator. In *42nd AIAA Plasmadynamics and Lasers Conference*, Volume N. A., pp. 1–8.

Swift, G. W. (1988). A liquid-metal magnetohydrodynamic acoustic transducer. *The Journal of the Acoustical Society of America* 83(1), 350-361.

Vogin, C. and A. Alemany (2007). Analysis of the flow in a thermo-acoustic MHD generator with conducting walls. *European Journal of Mechanics-B/Fluids* 26(4), 479-493.

Yamada, K., T. Maeda, Y. Hasegawa and Y. Okuno (2006). Two-dimensional numerical simulation on performance of liquid metal MHD generator. *Electrical Engineering in Japan* 156(1), 25-32.

Yamada, K., T. Maeda, Y. Hasegawa and Y. Okuno (2007). Three-dimensional numerical analysis of a liquid metal MHD generator. *Electrical Engineering in Japan* 160(3), 19-26.

Yamaguchi, H., X. D. Niu, and X. R. Zhang (2011). Investigation on a low-melting-point Gallium alloy MHD power generator. *International Journal of Energy Research* 35(3), 209-220.

Yohanis, Y. G., J. D. Mondol, A. Wright and B. Norton (2008). Real-life energy use in the UK: How occupancy and dwelling characteristics affect domestic electricity use. Energy and Buildings 40(6), 1053-1059.